Journal of Catalysis 404 (2021) 371–382

Contents lists available at ScienceDirect

Journal of Catalysis

journal homepage: www.elsevier.com/locate/jcat

The capping agent is the key: Structural alterations of Ag NPs during CO_2 electrolysis probed in a zero-gap gas-flow configuration

Menglong Liu [a,b], Ying Kong [a,b], Huifang Hu [a], Noémi Kovács [a], Changzhe Sun [a,b], Iván Zelocualtecatl Montiel [a], María de Jesús Gálvez Vázquez [a], Yuhui Hou [a,*], Marta Mirolo [c], Isaac Martens [c], Jakub Drnec [c], Soma Vesztergom [a,d,*], Peter Broekmann [a,b,*]

[a] University of Bern, Department of Chemistry, Biochemistry and Pharmaceutical Sciences Freiestrasse 3, 3012 Bern, Switzerland
[b] National Centre of Competence in Research (NCCR) Catalysis, University of Bern Freiestrasse 3, 3012 Bern, Switzerland
[c] European Synchrotron Radiation Facility, Experimental Division, Avenue des Martyrs 71, 38000 Grenoble, France
[d] Eötvös Loránd University, Department of Physical Chemistry Pázmány Péter sétány 1/A, 1117 Budapest, Hungary

ARTICLE INFO

Article history:
Received 16 August 2021
Revised 1 October 2021
Accepted 13 October 2021
Available online 21 October 2021

Keywords:
Power to value
Carbon dioxide electroreduction
Catalyst degradation
Particle sizing
Scanning electron microscopy
Wide-angle X-ray scattering

ABSTRACT

We apply silver nanoparticles (Ag NPs) as catalysts of CO_2 reduction in a zero-gap gas-flow electrolyser. Ag NPs stabilized by different ligands —branched polyethylenimine (BPEI), polyvinylpyrrolidone (PVP), polyethylene glycol (PEG), and citrate— are used in the experiments. The as-prepared NPs have almost identical initial size distributions, yet their catalytic performance, in terms of achievable current and CO selectivity, is different. During electrolysis all Ag NPs exhibit unambiguous morphology changes; the degradation pathway they follow, however, markedly depends on the chemical nature of the capping agent stabilizing them. Scanning electron micrographs obtained before and after constant-charge electrolyses carried out at different potentials reveal that amongst the studied ligands, BPEI seems to be the most effective stabilizer of Ag NPs; in turn, however, BPEI also limits CO formation the most. In case of PVP, mostly corrosion (particle shrinkage) is observed at practically relevant electrolysing potentials, while the application of PEG leads more to particle coalescence. Ostwald ripening seems to appear only at high applied (H_2 forming) potentials in case of the three afore-mentioned ligands while in case of citrate it becomes significant already at mild (CO forming) voltages. By studying the effects of capping agent removal and exchange we demonstrate that apart from ligands directly attached to the Ag NPs, also the excess of capping agents (adsorbed on the electrode surface) plays a decisive role in determining the extent and mode of catalyst degradation. The results of SEM-based particle sizing are also confirmed by synchrotron based wide-angle X-ray scattering measurements that provide further insight into the evolution of crystallite size and lattice strain in the applied Ag NPs during electrolysis.

1. Introduction

The electrochemical reduction of CO_2 into value-added products is a quickly developing field of electrocatalysis, mostly because it opens new perspectives in front of climate change mitigation [1]. Due to the considerable thermodynamic stability of carbon dioxide, the electrochemical CO_2 reduction reaction (CO_2RR) requires high negative potentials, and the application of catalyst materials that favour CO_2RR over the competing hydrogen evolution reaction (HER). The design of new catalyst materials that not only meet this requirement, but can also selectively direct CO_2RR towards the formation of a desired product at suitable rate and at low energy cost has thus become the forefront of electrochemical research in the past 20 years [2].

Although examples to the contrary already exist [3], metals or metal oxides (either in bulk [4], foam [5], or nanoparticulate [6] form) are still considered as catalysts of first choice for CO_2RR. While on bulk metal electrodes with large planar surfaces it is primarily the chemical nature of the metal [4] that determines the

* Corresponding authors at: University of Bern, Department of Chemistry, Biochemistry and Pharmaceutical Sciences, Freiestrasse 3, 3012 Bern, Switzerland (Y. Hou and P. Broekmann); Eötvös Loránd University, Department of Physical Chemistry, Pázmány Péter sétány 1/A, 1117 Budapest, Hungary (S. Vesztergom).

E-mail addresses: menglong.liu@unibe.ch (M. Liu), ying.kong@unibe.ch (Y. Kong), huifang.hu@unibe.ch (H. Hu), noemi.kovacs@unibe.ch (N. Kovács), changzhe.sun@unibe.ch (C. Sun), ivan.zelocualtecatl@unibe.ch (I. Zelocualtecatl Montiel), maria.galvez@dcb.ch (M.J. Gálvez Vázquez), yuhui.hou@unibe.ch (Y. Hou), marta.mirolo@esrf.fr (M. Mirolo), isaac.martens@esrf.fr (I. Martens), jakub.drnec@esrf.fr (J. Drnec), vesztergom@chem.elte.hu (S. Vesztergom), peter.broekmann@dcb.unibe.ch (P. Broekmann).

https://doi.org/10.1016/j.jcat.2021.10.016
0021-9517/

majority product (CO, formate, hydrocarbons, alcohols), in case of catalysts with nanosized features (nanoparticles or hierarchic foams) also the nanoscale structure has a pivotal role in determining selectivity [6,7]. In case of Cu nanoparticles (NPs), for example, a direct correlation between particle size and product distribution has already been established [8], and also for other metallic NPs (like Sn [9] or Ag [10]) intense research has been carried out to correlate the activity and selectivity of nanoparticulate catalysts to their morphology and physical structure. To use metals (or their oxides) in a nanoparticulate form for the catalysis of the CO_2RR is a very straightforward approach especially because of the many facile synthesis routes available that allow the design of NPs with fine-tuned catalytic properties.

Using metals in a nanoparticulate form for the catalysis of CO_2-RR has the obvious advantage that comes with the low raw material cost — small sized NPs can be applied in a relatively low loading to achieve an already considerable current of CO_2 reduction [5]. A significant drawback of nanoparticulate catalysts stems, however, also from the small size of NPs, which makes them thermodynamically unstable. Maintaining the stability of NPs under the operating conditions of electrolysis, that is, at high applied potentials, strong flow of current and intense gas formation, thus becomes a key question of research. In other fields of electrocatalysis (*e.g.,* in fuel cell research [11]) the degradation of catalyst NPs is well studied. In relation to CO_2RR on the other hand, only a few researchers seem to place emphasis on elucidating possible degradation mechanisms [9,10,12–16].

Ag is considered an appealing catalyst material for CO_2 reduction because it produces a single yet very sought-after product over a broad potential window and under different operating conditions: CO. CO is a remarkably versatile precursor of the production of synthetic fuels [17], and industrial applications already exist, for example, for the coupling of CO_2-to-CO/water-to-H_2 electrolysers to a fermentation module where CO and H_2 are converted to butanol and hexanol with high carbon selectivity [18]. In addition, the two-electron transfer required by the CO_2-to-CO conversion provides a large profit margin compared to other multiple-electron transfer products requiring larger energy inputs [17].

While in existing industrial electrolysers Ag is usually applied in a bulk form for the production of CO [18], it was recently shown in lab scale experiments that when Ag is used in a nanoparticulate form, stable CO formation can be achieved over a much broader potential window, and thus better conversion metrics can be achieved compared to the case when electrolysis is carried out on planar Ag cathodes [10].

In a recent study we made the first step in the direction of upscaling towards practical application by using Ag NPs as catalysts of CO_2RR in a zero-gap gas-flow electrolyser unit [15]. Zero-gap gas-flow electrolysers allow the realisation of large current densities ($\gg$300 mA cm^{-2}, normalized to geometric cathode surface area) and create an ideal playground for catalyst stability testing under harsh operating conditions.

The use of capping agents is essential in Ag nanoparticle synthesis as they control the shape and size of the grown nanoparticles, and prevent their aggregation over time [19]. Capping agents usually achieve long-term stabilization of the particle size [20] either by steric hindrance (such ligands usually have bulky protecting groups) or by an electrostatic repulsion between ligands bearing the same charge (such capping agents are usually ionic species). While essentially both types of ligands can work well in stabilizing NPs in dispersion, they both have significant drawbacks when it comes to fixing the NPs on an electrode surface and using them as electrocatalysts. In such cases NPs stabilized by charged ligands are often found to quickly agglomerate either due to screening effects arising from high ionic strengths or as a result of the electric field of the working electrode. NPs stabilized by steric hindrance are usually more stable, however in this case the strong adsorption of ligands often blocks the access of reactants to the NPs, leading to an overall decrease of the catalytic activity.

The structural changes metallic NP-based catalyst layers undergo in the course of the catalysed process can take many forms, including the *detachment* of particles from the support (which ultimately results in catalyst loss), the *corrosion* of the NPs (leading to an overall decrease of the average nanoparticle size), the *aggregation* of NPs on the catalyst support (leading to the formation of larger particles) and the phenomenon known as Ostwald ripening (as a result of which some particles grow larger on the expense of smaller ones disappearing). These structural changes (an illustration is shown in Fig. 1) all result in distortions of the particle size distribution of the NPs, and as such, they are commonly referred to as means of *degradation* — practically regardless to whether they have any measurable effect, either negative or positive, on the observed catalytic performance.

In practical electrolysers degradation rarely takes a single route, and in most cases it is a combination of several of the above-described degradation phenomena that determines the fate of catalyst NPs. The means and extent of degradation heavily depends on the operating conditions of the electrolyser (voltage and current, the intensity of gas formation, etc.), as well as on the chemical nature of the stabilizing (capping) agents applied either during the synthesis of the NPs or later for the formulation of the catalyst ink.

As capping agents not only adsorb on the surface of the NPs but also on the (usually carbon) cathode support, they may also play a decisive role in determining the surface adherence and the mobility of the NPs. While strongly bonding capping agents may preserve the initial particle size distribution of the NPs more efficiently than others, such ligands may also decrease catalytic performance by blocking the access of reactants to active catalyst sites. In such cases, the onset of "degradation" can even have an unexpected positive effect on the performance of electrolysis, as it can enable the participation of new, previously unaccessible sites in the catalysed process [21]. Apart from such exceptions, however, the degradation of NPs usually manifests in a long-term loss of the catalytic performance. This is primarily due to a loss of the active catalyst surface area that accompanies all degradation modes (including corrosion that often leads to the detachment of the smaller particles). A secondary degradation effect that may also account for performance losses is related not to the changing size distribution of the particles, but rather to a consequence of this: an internal structural change of the NPs, during which the (from a catalytic point of view, highly active) open crystalline sites re-organize to less ordered and more compact amorphous structures.

In this study we use Ag NPs capped by different ligands — branched polyethylenimine (BPEI), polyvinylpyrrolidone (PVP), polyethylene glycol (PEG), and citrate— with an initially narrow size distribution centred at $\sim$ 40 nm for the preparation of catalyst inks that we disperse on a gas diffusion layer. The thus prepared Ag NP GDE (Fig. 2) is in direct contact with the anion exchange membrane of the zero-gap gas-flow electrolyser (see also Figure S1 of the Supporting Information) that contains an electrolyte solution only on the anode side. The reactant gas (CO_2) is directly fed by a constant flow to the GDE, and the configuration does not only assure reduced ohmic losses but it also attenuates complications that arise from poor membrane hydration and electrode flooding at high current densities [15].

We show that in case of all four applied capping agents, the efficiency of CO_2RR considerably drops over time in a manner that is similar for all capping agents. While this performance loss, occurring due to the formation of carbonate plaques at high current densities over the electrode surface, is not a direct result of the structural changes that catalyst NPs suffer during electrolysis, the zero-gap gas flow cell still provides means to study the morpholog-

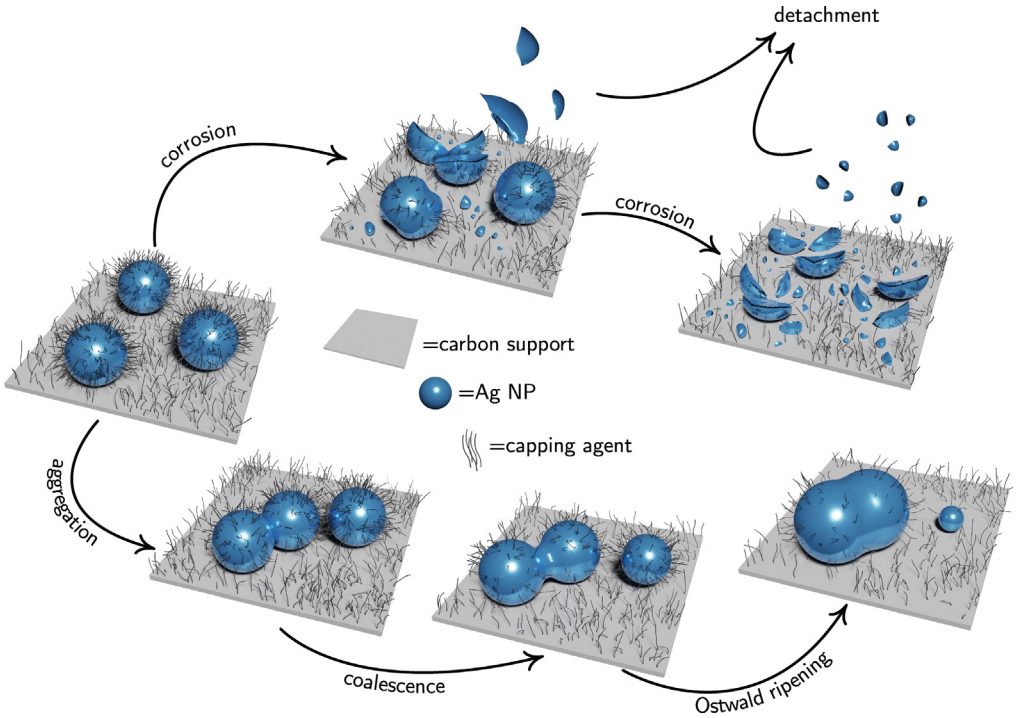

Fig. 1. Degradation pathways of Ag NPs used for CO_2RR.

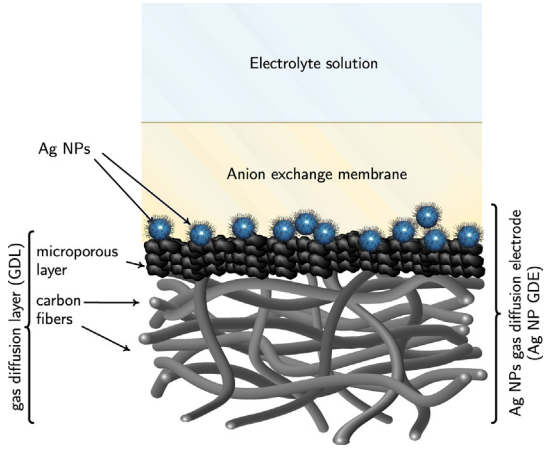

Fig. 2. The gas diffusion electrodes (Ag NP GDEs) used in this study are formed by drop-casting an Ag NPs containing catalyst ink on a gas diffusion layer (GDL). The latter is a bilayer structure consisting of a macroporous backing material (carbon fiber paper support) and a carbon-based microporous layer. The Ag NP GDE is separated by an anion exchange membrane from the electrolyte solution that contains the anode and a reference electrode.

ical changes of Ag NPs during intense CO_2RR/HER stressing. Following a removal of the formed carbonate plaques by careful dip-washing, structural changes can be investigated by a set of state-of-the-art nanoparticle characterization techniques including scanning electron microscopy (SEM) and wide-angle X-ray scattering (WAXS) measurements. These methods can clearly demonstrate that depending on the nature of their stabilizing ligands, Ag NPs undergo different degradation pathways on the course of electrolysis. By a set of ligand removal and exchange experiments we also demonstrate that apart from ligand molecules directly attached to the NPs, ligands adsorbed on the supporting carbon matrix also play a role in determining the dominant degradation mode.

2. Experimental Section

Preparation of the Ag NPs-containing catalyst ink. To prepare the carbon-supported Ag NP catalyst ink, 0.25 cm^3 of the as-received parent catalyst suspension (NanoComposix, Ag mass concentration of 1 mg cm^{-3}) was diluted to 0.55 cm^3 by the addition of Milli-Q water. A second suspension (volume: 0.44 cm^3) was made by dispersing carbon black (Vulcan XC 72r, Cabot) in isopropanol (VLSI Selectipur, BASF SE, Ludwigshafen, Germany) in a 0.1 mg cm^{-3} concentration. Both suspensions were sonicated separately for 10 and 30 min, respectively, following which the suspensions were intermixed and, after the addition of 10 $\mu\ell$ Nafion solution (5% Nafion, 15–20% water, Sigma–Aldrich), the new suspension was sonicated for further 10 min. The same ink preparation protocol was applied to all four nanoparticulate catalysts used herein. BPEI, PVP, PEG and citrate-capped Ag NPs with an average particle size of $\sim$ 40 nm were purchased from a supplier (NanoComposix) and were used directly for the ink preparation. In order to carry out experiments by removing some of the excess PVP capping agent, the parent Ag NP suspension was first subjected to centrifugation (at 35 000 rpm, 40 min, Beckmann Coulter ultracentrifuge, SW60 rotor). This treatment allowed for a separation of the surfactant-capped Ag NPs and the free surfactants that remained, at least to a large extent, in the liquid (aqueous) phase. The separated Ag NPs were then suspended in Milli-Q water to keep the Ag concentration the same as that of the parent suspension, and the ink preparation protocol described above was followed. The separated Ag NPs and the aqueous matrix phase were both subjected to a total organic carbon concentration (TOC) analysis with the aim to estimate the amount of surfactants that is either attached to the Ag NPs or is present in solution (see Table S5 in Supporting Information).

Preparation of the Ag NP GDEs. GDEs were formed by drop-casting 40 $\mu\ell$ of either one of the above-described catalyst inks onto the masked hydrophobic surface of a GDL (H23C8, FuelCellStore, see Figure S2 of the Supporting Information for SEM charac-

terization). The GDE was in contact with the membrane through a circular opening with a diameter of 3 mm, and the corresponding geometric area (7.07 mm^2) is used for the surface normalization of current to current density. The catalyst ink was percolated through the porous body of the GDE by a vacuum filtration system placed on the backside of the electrode, followed by drying at ambient conditions. The resulting mass loading was in the range of (43±5) $\mu g\ cm^{-2}$, as confirmed by inductively coupled plasma mass spectrometry (ICP–MS, see Table S1 in Supporting Information for detailed loading data).

Assembly of the gas flow-cell. The assembly and main components of the zero-gap gas-flow cell employed in this work have been described elsewhere [15]. The cell (see also Figure S1 in Supporting Information) consists of a stainless steel body with the gas flow channels used to feed the CO_2 from the backside of the prepared Ag NPs GDE mounted on the outermost location of the central portion. Other components incorporated into the cell include a current collector and a gas inlet and outlet to control the supply of the CO_2 reactant (99.999%, Carbagas, Switzerland) and analysis of gaseous products, respectively. All the CO_2 reduction experiments were set up by placing a freshly prepared Ag NPs GDE on top of the gas flow channels, with its catalyst modified surface facing upward. Subsequently, a new hydroxide-functionalised Sustainion alkaline membrane (X3750 RT, Dioxide materials) and a poly-(tetrafluoroethylene) anolyte compartment were placed on top of the GDE. A clamp was then used to guarentee cell tightness and mechanical stability. 10 cm^3 of 2.0 mol dm^{-3} KOH was used as electrolyte for the anolyte compartment. An Ag|AgCl|3 mol dm^{-3} KCl electrode (double junction design, Metrohm) was used as a reference, and an Ir wire (99.9%, MaTeck Material-Technologie & Kristalle GmbH, Germany) separated by a glass frit was used as a counter electrode. Note that the PTFE anolyte compartment has a central orifice (of 3 mm diameter, corresponding to a geometric surface area of 7.07mm^2) in its bottom part that provides direct contact between the electrolyte and the underlying anion-exchange membrane, while the Ag NPs GDE is prevented from direct contact with the supporting anolyte. During electrolysis, a humidified CO_2 stream (16 $cm^3\ min^{-1}$) was continuously fed through the gas flow channels of the stainless steel cell body, adjacent to the GDE.

Electrochemical measurements and product distribution studies. An ECi-200 potentiostat (Nordic Electrochemistry) was used to perform all electrolysis experiments. The electro-generated gaseous products (CO and H_2) were determined by means of on-line gas chromatography (SRI Instruments) in fixed (10 or 4 min) time intervals. The electrolyte solution was also analysed after full electrolyses, to check for any soluble products formed, by means of ion exchange chromatography (Metrohm Ltd., Switzerland). As formate (in different amounts, see Table S3 in Supporting Information) was found as the sole dissolved product in the electrolyte solution, it was assumed that whenever the GC-based detection of volatile products could not account for a 100% of Faradaic efficiency, the rest of the passed current was turned into formate production.

Electron microscopy measurements. For the morphological characterization of the Ag NPs on GDEs, a Zeiss Gemini 450 scanning electron microscope equipped with an InLens secondary electron detector and a back-scattering detector was used. An accelerating voltage of 5 kV and a current of 120 pA were applied at a working distance of 3.8–4.2 mm. Using the Smile View software for particle sizing, ca. 500–900 particles were analysed per experimental setting for the creation of the particles size distribution shown in Figs. 7, 9 and 10. The particle size was defined as the longest measurable dimension in case of anisotropic NPs, see Figure S13 in the Supporting Information. To acquire EDX point spectra and 2D surface mappings of selected samples, the AZtec 4.2 software (Oxford Instruments) was used. An acceleration voltage of 10 kV and a current of 500 pA were applied at a working distance of 8.5 mm for EDX measurements. For high-angle annular dark-field scanning transmission electron microscopy (HAADF–STEM) combined with energy-dispersive X-ray spectroscopy (EDX), a Talos F200X (Thermo Fisher Scientific) instrument equipped with a SuperEDX detector was used with an acceleration voltage of 200 kV.

Contact angle measurements. Contact angle measurements were carried out using a Krüss Advance Drop Shape Analyzer DSA25 (Krüss GmbH, Hamburg, Germany). Electrodes were mounted on a flat stage and water drops (milli-Q water, 1.4 μL) were deposited at room temperature.

Synchrotron Wide-Angle X-ray Scattering (WAXS) measurements. Crystallite size and microstrain were measured via WAXS measurements at the ID31 beamline of the European Synchrotron Radiation facility (ESRF) in Grenoble, France. The high energy X-ray beam (75 keV) was focused on the Ag NP GDEs, and the scattered signal was collected using a Dectris Pilatus CdTe 2 M detector positioned 520 mm behind the sample. The energy, detector distance and tilts were calibrated using a standard CeO_2 powder and the 2D diffraction patterns were reduced to the presented 1D curves using the pyFAI software package [22]. Rietveld refinement of the WAXS patterns was performed to extract the phase structure, crystallite size, lattice parameter and microstrain using the cubic *Fm–3 m* structure of Ag metal and the GSASII software [23], see Figure S14 in Supporting Information for a representative fit. The instrumental parameters were determined by the refinement of a CeO_2 standard sample. Air scattering was removed from each pattern. The measurement consists in a height scan acquiring WAXS pattern at different positions in the sample. The pattern of the GDE is considered as background and removed for each sample. The fitting is performed using crystallites of uniaxial orientation along the (111) direction.

White light interferometry (WLI) analysis. The mesoscopic surface morphology of the Ag NP GDEs was analyzed by means of white light interferometry (Contour GT, Bruker, see Figure S5). Vision64 software (Bruker) was used for operating the instrument and for data analysis.

Inductively coupled plasma mass spectrometry (ICP-MS). GDE samples were immersed for 24 h in 1 cm^3 HNO_3 (69.3%, BASF SE, Ludwigshafen, Germany) to dissolve all Ag NPs. The resulting solutions were diluted with 3% HNO_3 solution by a factor of 500 and were then fed into a NExION 2000 ICP-MS instrument (Perkin Elmer) to obtain the Ag mass loading of the electrodes (see Tables S1 and S4 in Supporting Information).

Total organic content (TOC) determination. To quantify surfactants in each solution, 100 $\mu\ell$ of free surfactant solutions obtained by centrifugation of Ag NP suspensions (0.25 mg cm^{-3}) and surfactant-capped Ag NP suspensions (0.25 mg cm^{-3}) which do not contain free surfactants were fed into a DIMATOC 2100 instrument (Dimatec, Essen, Germany). The organic compounds were oxidized at 850 °C with Pt as catalyst to CO_2/NO. Non-dispersive infrared (NDIR) gas sensor with a reflective diffuser and a chemiluminescence detector were used to detect CO_2 and NO, respectively.

3. Results and Discussion

Characterization of the as-prepared Ag NP GDEs. Essentially regardless to the nature of the stabilizing ligand (BPEI, PVP, PEG or citrate), all our studied Ag NP GDEs exhibited very similar physical characteristics (Fig. 3). Representative SEM images of (PVP-capped) Ag NP GDEs are shown in Fig. 3a and c, revealing isotropic and uniformly dispersed NPs with an almost uniform particle size

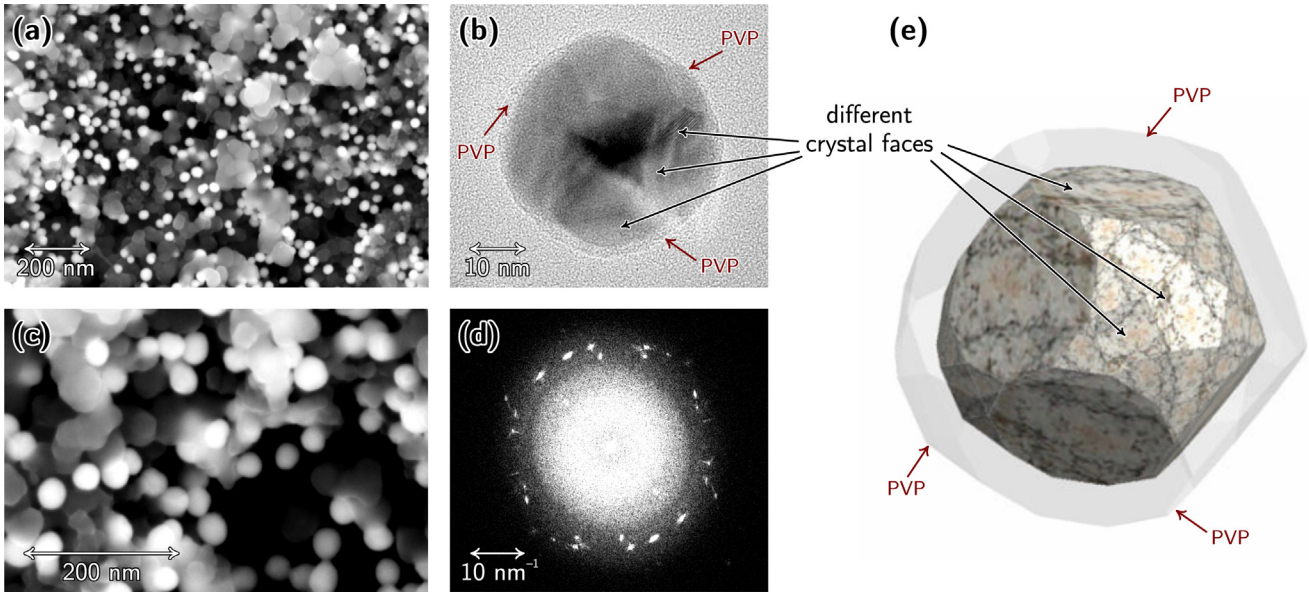

Fig. 3. Representative top-down SEM images (a, c) of PVP-capped Ag NPs dispersed on the carbon microporous layer of the GDE. The HR–TEM image (b) of an individual PVP-capped Ag NP, and its Fourier-transformed representation (d) demonstrate the polycrystalline nature of the nanoparticle, exhibiting different crystalline domains. Schematic drawing of the PVP-capped Ag NP is shown in (e). For a complete (top-down) SEM and TEM view of GDEs prepared by the use of Ag NPs capped with different ligands, see Figure S3 and S4 in the Supporting Information.

of about 37 nm. The HR–TEM image and the corresponding FFT representation of an individual PVP-capped Ag NP, shown in Fig. 3b and d, reveal the polycrystalline nature of the NPs. The drawing in Fig. 3e, inspired by the result of electron micrography, attempts to show a single Ag NP in three dimensions. Similar initial states were found in the case of Ag NPs capped by other ligands (BPEI, PEG and citrate). Independently of the nature of the capping agent used by the provider (NanoComposix) for the synthesis of the studied Ag NPs, we found that all NPs used in this work are of an (almost) spherical shape, as shown in Fig. 3e, and that the NPs exhibit no preferential faceting. The uniformly dispersed particles were isotropic but polycrystalline, and their average size was between 30 and 40 nm in all cases. Corresponding SEM and TEM images of all four types of surfactant-capped Ag NPs are shown in Figures S3 and S4, respectively, of the Supporting Information, where white-light interferometry images (top view of the catalyst layer, Figure S5), as well as cross-sectional (side view) SEM and EDX images (Figure S6) can also be found. The latter show that the majority of Ag NPs does not penetrate the GDE, and remains dispersed on top of the microporous layer.

CO_2RR/HER stressing. In order to study the electrochemical performance of Ag NP GDEs, potentiostatic electrolyses in the configuration shown in Fig. 2 were carried out at three different applied potentials. Keeping comparability in mind, all electrolyses were performed until the same amount of charge (300 C cm^{-2}, normalized to the geometric surface area of the circular opening of the zero-gap cell) passed through the electrolyser. The product distribution (that is, the partial current densities of CO and H_2 formation, see the dashed lines) were reconstructed on the basis of on-line GC measurements at given fixed time intervals, shown by the dots in Fig. 4.

As the amount of CO and H_2 detected by on-line GC measurements did not account for a 100% Faradaic efficiency, contents of the electrolyte were analysed post-electrolysis by ionic liquid chromatography (IC), which revealed a significant amount of formate production at each setting (see Table S3 in Supporting Information). As no water-soluble products apart from formate were detected after electrolysis by IC, it is safe to assign the missing fraction of the current density (hatched areas in Fig. 4 labelled "rest") to the production of formate [15,24].

Fig. 4 reveals a rather similar behaviour of three out of four studied catalysts. Namely, the PVP-, PEG- and citrate-capped Ag NPs all seem to exhibit a remarkable selectivity towards the production of CO, although especially at larger electrolysing potentials this selectivity, as well as the overall current, significantly decrease with time. That the catalytic performance of these NPs seems not to depend significantly on the nature of the applied capping agents suggests that already at initial stages of the electrolysis at least a partial removal of the capping shell from the surface of the NPs may have occurred, leaving catalytically active sites available to participate in CO_2RR [13,16,21].

As for BPEI-capped Ag NPs, both the overall current and the selectivity of CO production are considerably smaller (essentially at all three applied potentials), and this observation can be explained by the exceptionally strong bonding interactions between the amino groups of BPEI and the Ag NPs. Due to this strong bonding it seems plausible to assume that the BPEI-capped particles remain at least partially inaccessible for the reactants of electrolysis. As a result, the observed performance loss is in turn also smaller compared to the case of NPs capped by other agents (PVP, PEG or citrate).

In case of all four types of NPs, a clear decrease is observed in both the Faradaic efficiencies of CO formation and the current density as a function of time (*i.e.*, charge) at each potential. The performance decay is especially rapid at the electrolysing potential of –2.354 V, where the Faradaic efficiency of CO formation very quickly drops due to intense hydrogen evolution. Although less severe, performance losses can also be observed in the cases of lower electrolysing potentials in Fig. 4. The question whether the observed performance loss has anything to do with the actual morphology changes of the NPs during the electrolysis immediately follows: we found, however, that although by SEM and WAXS investigations significant morphology changes can indeed be monitored, these structural alterations are not the main cause of the performance losses observed in Fig. 4.

The obvious decrease of the overall current density and the relative selectivity of the catalyst NPs to produce CO is rather connected to another phenomenon, namely the formation of a mostly potassium carbonate-based precipitate over the GDE. This

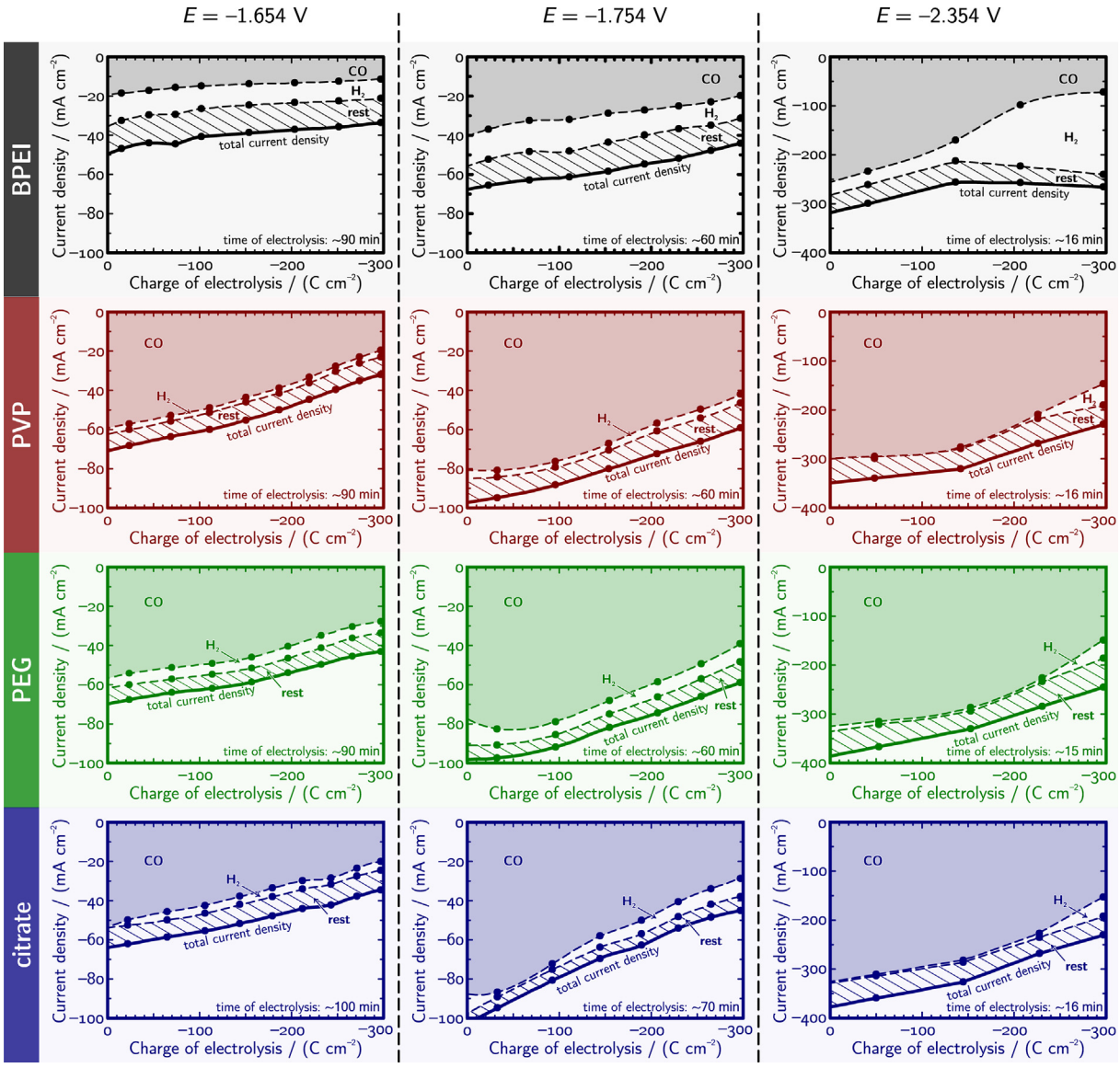

Fig. 4. Total current densities (full thick curves) plotted as a function of the passed charge density at different constant electrolysis potentials (measured vs. Ag/AgCl) for differently capped Ag NP GDEs. Electrolyses were stopped in all cases after the same amount of charge (−300 C cm^{-2}) was passed through the electrode. Shaded areas and dashed curves show the product distribution as reconstructed by GC measurements at different times (indicated by dots). Note that CO and H_2 were the only GC-detectable products that however did not account for a 100% of Faradaic efficiency. The "rest" of the current (hatched area in the graphs) can most probably be assigned to formate production (see the text and Tables S2 and S3 in Supporting Information for more details).

serious effect —that however does not hinder the observation of actual morphology changes on the nanoscale— is exemplified in Fig. 5.

As shown in Fig. 5, the pristine GDL we start out from (see Fig. 5a for a photograph) exhibits a clear surface, and the top- and side-view SEM images (Fig. 5b and c) reveal the expected structure of the surface microporous layer and the underlying carbon fibers. The surface of the top microporous layer is hydrophobic, as demonstrated by contact angle measurements on a sessile water drop, Fig. 5d. The EDX mapping analysis (Fig. 5q) reveals only carbon and fluorine signals in the elemental composition (the latter arises due to the PTFE treatment of the GDL applied by the manufacturer).

Fig. 5e shows a photograph of the (PVP-capped) catalyst ink drop-cast on the GDL. The circular area that will serve as the active cathode surface of the electrolyser (this will be in direct contact with the membrane) is shown here by a dashed circle. The catalyst NPs are clearly visible by SEM (Fig. 5f) and EDX-based elemental mapping (Fig. 5g) confirms that the NPs are clearly composed of Ag. Drop-casting the catalyst ink on the surface does not significantly decrease the hydrophobicity of the GDE (Fig. 5h), while in the EDX spectrum (Fig. 5h) the signal of Ag clearly appears.

When this GDE is subjected to CO_2RR/HER stressing, the formation of a potassium carbonate/bicarbonate based precipitate immediately becomes visible also to the bare eye, as shown in the photograph of Fig. 5i. An SEM image of the formed carbonate plaque is shown in Fig. 5j, and the elemental composition map of Fig. 5k reveals K as a major component of this plaque. Due to the formation of the carbonate precipitate the surface of the GDE becomes hydrophilic (Fig. 5l) and the signals of both K and O appear in the EDX spectra of Fig. 5q.

That the formed carbonate plaque is beyond doubt responsible for the performance losses observed before in Fig. 4 can be proven by a set of "recovery" experiments. These show (see Figure S12 in

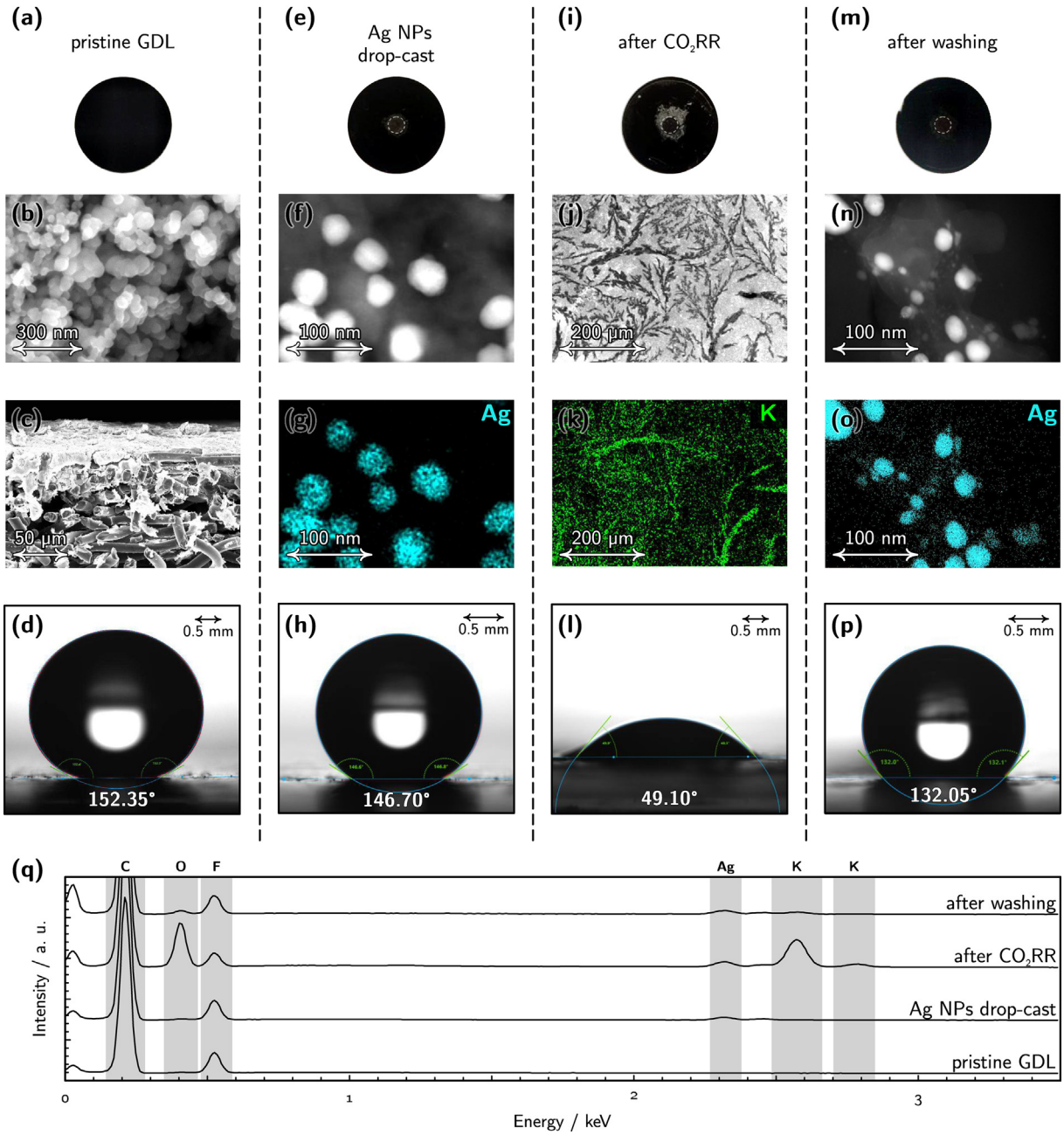

Fig. 5. The characteristic features of a pristine GDL significantly change after surfactant-capped Ag NPs are drop-cast on it, the thus prepared GDE is used for electrolysis, and finally, after the carbonate precipitate formed during CO_2RR/HER stressing is washed away. See the text for an exact description of each panel, and Figures S7–S11 of the Supporting Information for more details.

Supporting Information) that following a removal of the carbonate layer by dip-washing, already used GDEs can almost completely regain their efficiency in a subsequent electrolysis.

As the formed carbonate plaque makes us unable to study the degradation of NPs during CO2RR/HER stressing, the carbonate precipitate was removed from the surface following electrolysis by careful dip-washing (see Figure S8 in Supporting Information for details). A photograph of the GDE following the dissolution of the carbonate plaque is shown in Fig. 5m, and the subsequently taken SEM images (Fig. 5n and o) clearly indicate that this cleaning method does leave the actual catalyst NPs intact (compare panels n and o with f and g in Fig. 5). The accuracy of the dip-washing method is also proven by EDX (Fig. 5q) showing that the K and O signals almost fully disappear and the Ag signal is regained after washing. That the dip-washing technique we used to remove the carbonate plaque from over the catalyst surface did not result in any significant catalyst (Ag) loss was confirmed by ICP–MS analysis (see Table S4 in Supporting Information).

Morphology changes of Ag NPs on GDEs studied by SEM. The reliability of the applied dip-washing method allowed us to apply SEM analysis in order to study the structural changes that the differently capped Ag NPs undergo during extensive CO_2RR/HER stressing. Representative SEM images of pre- and post-electrolysis (dip-washed) samples are shown in Fig. 6 for the studied four types of surfactant-capped Ag NP catalysts. The histograms shown in Fig. 7 were prepared by manually processing several micrographs similar to those shown in Fig. 6: the size of each NP, regardless

to form, was determined by measuring its longest dimension as illustrated by Figure S13 in the Supporting Information.

Expectation ranges of the particle sizes (mode±deviation) were determined by making the histograms shown in Fig. 7 subject to probability distribution fitting. Histograms exhibiting a single mode were fitted by log-normal distributions yielding an unsymmetrical (skewed) expectation range, while in case of bimodal distributions the linear combination of two (symmetric) Gaussians were used to describe our datasets. Expectation ranges for the average particle size are specified for all panels of Fig. 7, making it apparent that the morphology of the Ag NPs evolved differently in case of the four different capping agents.

In case of BPEI, the observed particle size distributions are bimodal both before and after electrolyses. Interestingly, the second characteristic particle size (corresponding to a smaller peak) is twice of the first one, which implies, taking into consideration that we used the longest measurable dimension for particle sizing, two-particle aggregates were present at the GDE surface, already before electrolysis. As also shown in Fig. 7, however, no significant change of the characteristic particle sizes are observed when BPEI-capped Ag NPs are exposed to electrolysis stressing at different potentials, and this is in agreement with the results of Fig. 4 that also show a relatively stable catalytic performance of BPEI-capped Ag NPs.

The situation is markedly different in the case of PVP-capped nanoparticles that, as shown in Fig. 7, tend to corrode during electrolysis. Corrosion in case of PVP-capped Ag NPs leads to a significant decrease of the characteristic particle size, as well as to a general broadening and a larger skewness of the distribution.

In the case of PEG, stressing by CO_2RR/HER seems to have rather the opposite effect. While the first characteristic particle size remains essentially unchanged, as a result of electrolysis a second peak becomes visible in the histograms, and the maximum of this peak is approximately twice of that of the first one. This is a clear hint [25] to that in case of PEG, particle coalescence is the most favoured mode of catalyst degradation (see also the micrographs of Fig. 6).

The general increase of particle sizes is also apparent in the case of citrate-capped Ag NPs, as shown in the last row of Fig. 7, although in this case no evolution of further, distinct modes are seen: the histograms, instead, get significantly broadened and skewed as a result of electrolysis. In this particular case we assume that due to the relative instability of the citrate shell at the applied (negative) potentials, the NPs quickly become almost totally unprotected [26]. As a result, their aggregation/coalescence becomes unhindered, and apart from the coalescence of neighbouring particles, also Ostwald ripening (either its two or three-dimensional form) occurs in this case [27,28].

To conclude, the SEM analyses seem to suggest that PVP-capped particles undergo more the corrosion pathway of degradation (Fig. 1), while PEG- and citrate-capped NPs tend more to aggregate, coalesce, and (especially in case of citrate) some form of Ostwald

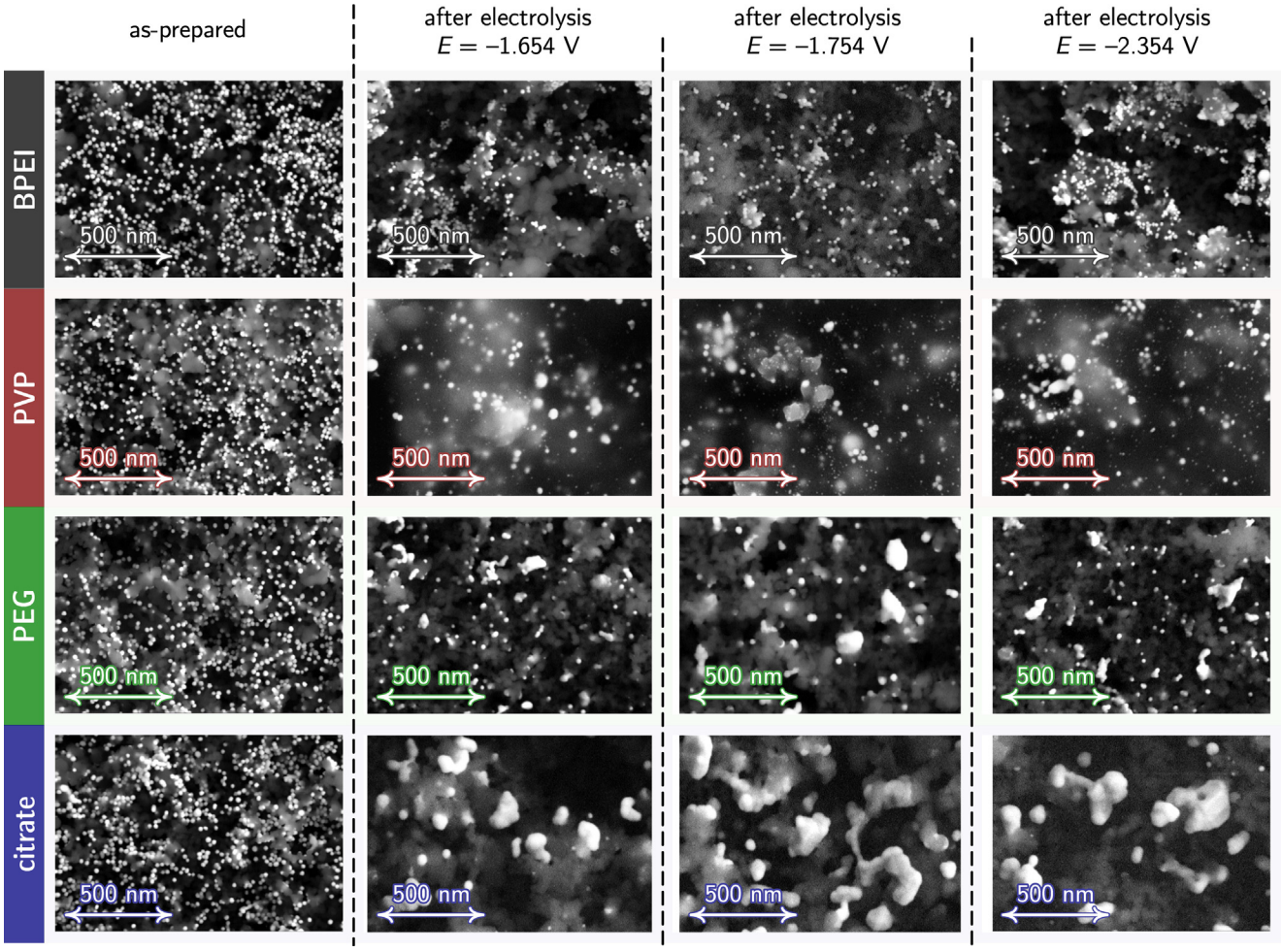

Fig. 6. Representative SEM micrographs of GDEs prepared using Ag NPs stabilized by different capping agents, recorded before ("as-prepared") and after constant charge electrolyses at different potentials (cf. to Fig. 4). These, as well as some other similar SEM images were used to construct the histograms shown in Fig. 7.

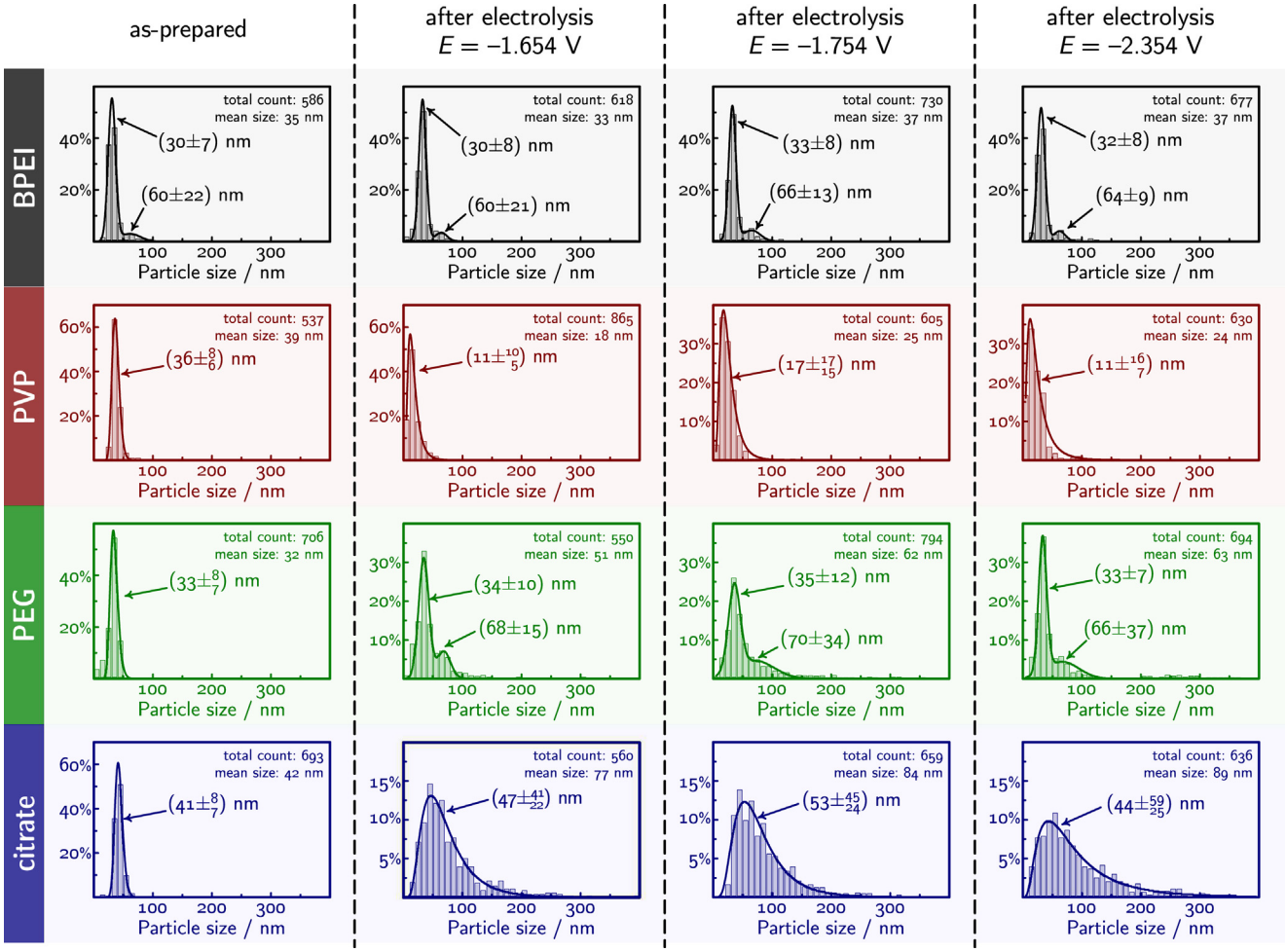

Fig. 7. Histograms showing the particle size distribution of Ag NPs, capped by different ligands, before and after electrolysis at a given potential. Expectation ranges of the particle size are shown for the fitted peak(s).

ripening also seems to take place. Amongst the studied capping agents, BPEI seems to be the most protecting one, as in this case no particular changes of the size distribution was observed when comparing post- to pre-electrolysis SEM images.

Morphology changes of Ag NPs on GDEs studied by WAXS analysis. The above picture can further be nuanced if we also use WAXS measurements to characterize the morphology changes of Ag NP catalysts during electrolysis (Fig. 8). The width of the WAXS peaks have two main contributions —apart from instrumental broadening—, and these are the size of coherently scattering domain (crystallite size) and microstrain (deviation from perfect order). These different characteristic parameters were determined by Rietveld fits of the diffraction pattern. Because the size determined by Rietveld fit maps crystallite sizes rather than full geometrical sizes, direct comparison between the WAXS and SEM-based analysis can reveal new insights about the degradation phenomena. First we note that using only the isotropic size model did not fit the data well. The fits improved significantly only after a size anisotropy had been included, implying that the nanoparticles have preferred growth orientation along the (111) direction (Fig. 8 and Figure S16 in Supporting Information). Along this direction, the crystallite size is about two times longer when compared to the short directions.

In the case of BPEI, the crystallite size is smaller than the particle size determined by the SEM analysis. This hints that the particles are composed from several crystallites, in agreement with the TEM observations. In this case the size does not change significantly, supporting the conclusions from the SEM analysis that the particles are stable during electrolysis. The microstrain shows a very low value for as-prepared NPs, but increases significantly for the samples measured after electrolysis. Given that the microstrain is a direct measure of internal disorder of the crystallites, the electrolysis seems to distort the local order which is typically linked to the increase of grain boundaries length. However, as in our case we do not observe any decrease in crystallite dimensions, the increase of microstrain should either be linked to surface phenomena caused by changes in the BPEI surface structure [29], or, alternatively, could be explained by some carbonate precipitates (that were not entirely removed by dip-washing) remaining adherent to the catalyst NPs (cf. to Fig. 5 exhibiting a small K signal even after washing).

The PVP case shows different behaviour. After electrolysis, the crystallite size increases in both directions, independently of the applied current, and the microstrain values increase moderately. This crystallite size increase is apparently opposite to the SEM-derived trend in particle size and the crystallites appear significantly larger than the physical size measured by SEM. This is caused by a broadening of the particle size distribution during electrocatalysis that is due to the formation of some amount of larger NPs while the average size shows a general decrease in the SEM measurements. It is of worth to note that while SEM results a number-weighted distribution, the diffraction amplitude is weighted by the volume of the NPs, therefore the crystallite size

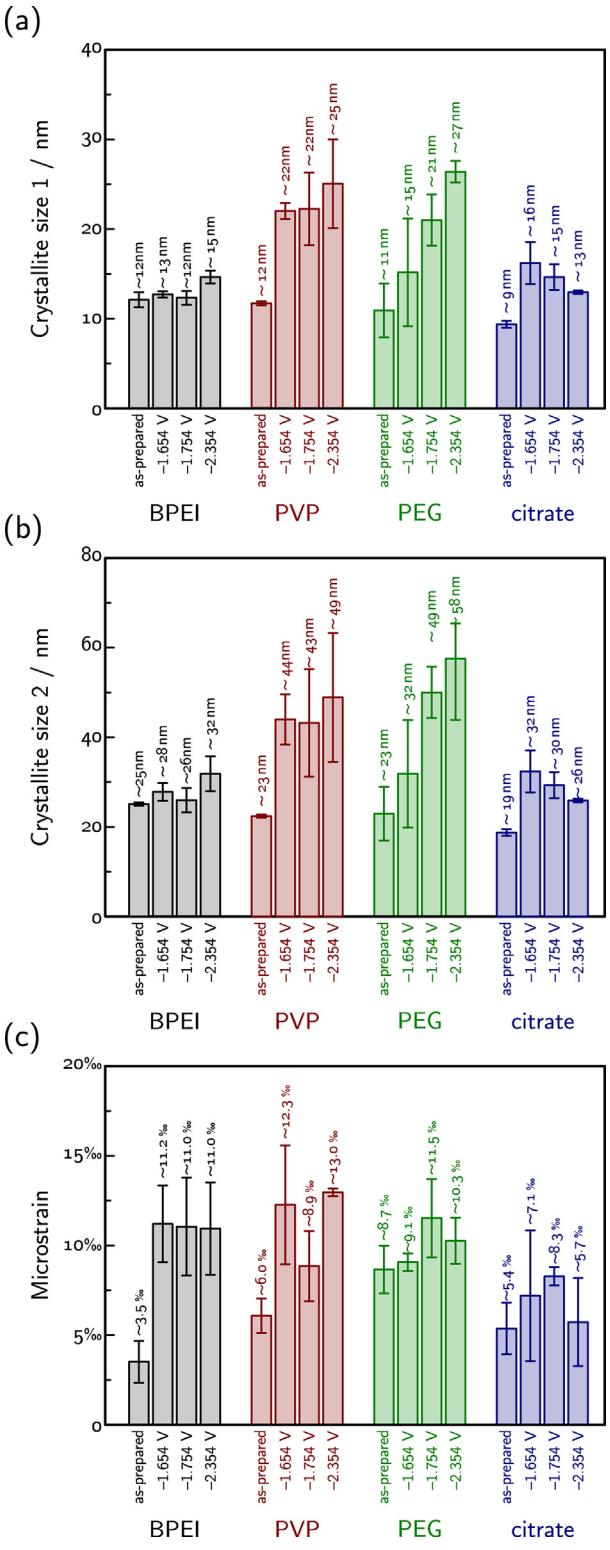

Fig. 8. Crystallite sizes (a, b) and microstrain (c) measured by WAXS of Ag NPs, capped by different ligands, before and after electrolysis at a given potential.

is much more sensitive to the appearance of larger NPs in the whole ensemble. This can result in crystallite sizes seemingly larger than the size of the NPs as determined by SEM using the distribution maximum. Based on the above observations we can conclude that apart from corrosion, that is a dominant pathway of the degradation of PVP-capped Ag NPs, Ostwald ripening also takes place in this case — and this causes both the increase of crystallite sizes (Fig. 8) and the broadening towards bigger sizes of the SEM-based size distribution (Fig. 7).

WAXS measurements on PEG-capped Ag NPs show a similar trend of increasing crystallite size, consistently with the appearance of bimodality in the SEM-based size distribution. PEG-capped NPs are not only aggregated, but the individual crystallites are also fused together through coalescence during electrolysis. The picture is somewhat different for citrate capped NPs that although as evidenced by SEM clearly undergo coalescence to a large extent during electrolysis, at the same time show only a moderate increase of the crystallite size. This is a hint to that the fusion of the NPs does not necessarily involve the merging of crystallites and that the enormously large Ag particles formed from citrate-capped Ag NPs during electrolysis (see, e.g, Fig. 6) can be composed of several distinct crystalline domains. The relatively low changes of microstrain observed in the case of PEG- and citrate-capped NPs are likely linked to the fact that the capping agent is only loosely bound to the surface of these NPs.

Ligand removal and exchange experiments. That in our investigations we saw the most severe degradation taking place in the case of citrate-capped Ag NPs can plausibly be explained by the fact that citrate stabilizes the NPs not by a steric effect as the other three studied ligands do, but by an electrostatic force. It can thus safely be assumed that under the operating conditions of electrolyses — that is, at high cathodic potentials— most of the negatively charged citrate ions will leave not only the surface of the NPs but they would also desorb from the surface of the carbon support. This can enhance the surface mobility of the particles, leading to their more rapid aggregation and then coalescence.

In order to check whether ligand molecules that may have remained adsorbed on the support in the three other (non-citrate) case have any role in determining the degradation pathway of the NPs, we designed a set of ligand exchange/removal experiments. These were based on separating the NPs from their parent dispersion by centrifugation, which left the majority of the capping agents —that would necessarily end up on the support surface during the GDE preparation— in the supernatant (see Table S5 and Figure S14 in Supporting Information). Filtering and re-dispersing the nanoparticles in Milli-Q water after centrifugation (see Section 2 for details) thus allowed us the (at least partial) removal of the carbon substrate-attached ligands or, if re-dispersion took place in the solution of another capping agent, the (again, at least partial) exchange of ligands.

The effect of ligand removal on electrolysis-induced degradation is shown in Fig. 9 for PVP-capped Ag NPs (this time, electrolysis took place at $E = -1.754$ V, see Figure S15a in Supporting Information for more details). We can see a notable difference if we compare this figure to the appropriate panels of Figs. 6 and 7: namely, that while the initial size distribution of the NPs is seemingly unaffected by the removal of excess PVP, the degradation pathway markedly changes. While in the previous case, when excess PVP was adsorbed on the carbon support layer, we primarily observed corrosion (and the change of the average particle size from around 39 to 25 nm), in Fig. 9 we see an increase of the average size (from 42 to 67 nm) and a significant broadening of the distribution. It seems to be a plausible assumption that the apparent coalescence we observe here was in the previous case hindered by support-adsorbed PVP, rendering the degrading NPs immobile. Alternatively, the removal of a significant portion of PVP from the surface of the NPs might have also lead to an increase of the average particle size by allowing quicker Ostwald ripening.

The role of support-adsorbed ligands can further be emphasized if we carry out a ligand exchange (as opposed to removal) experiment with citrate-capped Ag NPs that we in this case after centrifugation re-disperse in a PVP solution. As shown in Fig. 10, this

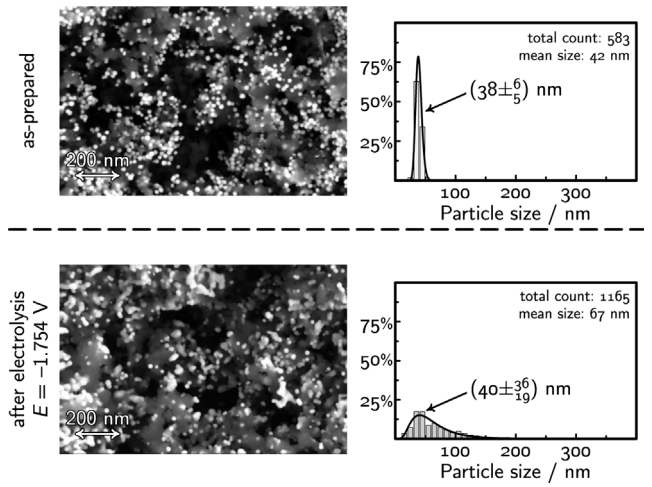

Fig. 9. The partial removal of the excess PVP from the catalyst ink results in less PVP adsorbed on the carbon support, facilitating more the aggregation (rather than the corrosion) of Ag NPs. (Cf. to Figs. 6 and 7).

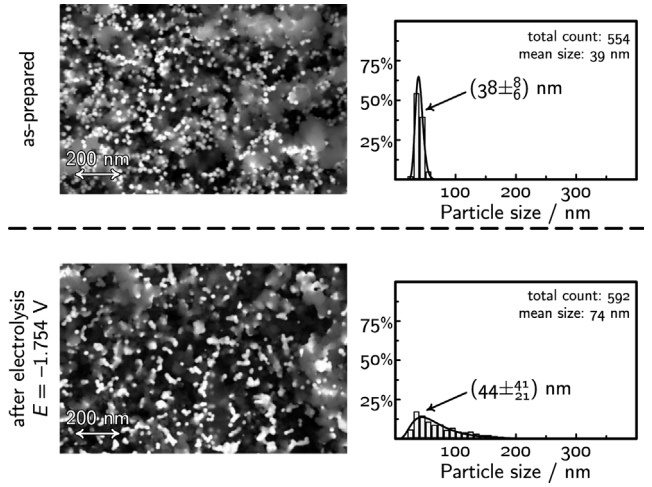

Fig. 10. The partial citrate → PVP ligand exchange in the catalyst ink results in more PVP adsorbed on the carbon support, somewhat hindering the coalescence degradation pathway otherwise observable for citrate-capped NPs. (Cf. to Figs. 6 and 7.).

can milden the coalescence of particles (otherwise characteristic for citrate-capped NPs, see Fig. 6 and 7), and this effect can also be explained by the adsorption of the extra PVP amount on the support surface, hindering the motion of the degrading NPs. (For more details of the electrolysis experiments, see Figure S15b of the Supporting Information.).

4. Conclusion

In this paper we used Ag NPs capped by different stabilizing ligands to prepare gas diffusion electrodes that we applied for CO_2 electroreduction in a zero-gap gas-flow electrolyser. This configuration allowed a high current stressing of the NPs. After careful cleaning of the GDE from the carbonate precipitates formed during electolysis, we compared SEM images of the catalyst NPs obtained before and after the high current testing, and made these subject to a statistical analysis.

We showed that amongst the studied capping agents, BPEI is the most protective one; in turn, however, it also limits CO formation the most. In case of PVP, mostly corrosion (particle shrinkage) was observed at practically relevant electrolysing potentials, while the application of PEG and that of citrate lead more to particle coalescence. In parallel with the SEM-based investigations, WAXS analysis was also used to follow the evolution of crystallite size and lattice strain during CO_2RR/HER stressing, and the results were compared to those of SEM mapping.

By studying the effects of capping agent removal and exchange we demonstrated that apart from ligands directly attached to the Ag NPs, also the excess of capping agents (adsorbed on the carbon support surface) plays a decisive role in determining the extent and mode of catalyst degradation.

Declaration of Competing Interest

The authors declare that they have no known competing financial interests or personal relationships that could have appeared to influence the work reported in this paper.

Acknowledgement

P. B. acknowledges financial support by NCCR Catalysis. S. V. acknowledges support from the National Research, Development and Innovation Office of Hungary (NKFIH grant FK135375). M. L., Y. K., H. H., and C. S. acknowledge the financial support by the Chinese Scholarship Council (CSC).

Appendix A. Supplementary material

Supplementary data associated with this article can be found, in the online version, at https://doi.org/10.1016/j.jcat.2021.10.016.

References

[1] D.R. Feldman, W.D. Collins, P.J. Gero, M.S. Torn, E.J. Mlawer, T.R. Shippert, Observational determination of surface radiative forcing by CO_2 from 2000 to 2010, Nature 519 (2015) (2000) 339–343, https://doi.org/10.1038/nature14240.

[2] D.T. Whipple, P.J.A. Kenis, Prospects of CO_2 utilization via direct heterogeneous electrochemical reduction, J. Phys. Chem. Lett. 1 (2010) 3451–3458, https://doi.org/10.1021/jz1012627.

[3] H. Coskun, A. Aljabour, P.D. Luna, D. Farka, T. Greunz, D. Stifter, M. Kus, X. Zheng, M. Liu, A.W. Hassel, W. Schöfberger, E.H. Sargent, N.S. Sariciftci, P. Stadler, Biofunctionalized conductive polymers enable efficient CO_2 electroreduction, Sci. Adv. 3 (8) (2017) e1700686, https://doi.org/10.1126/sciadv.1700686.

[4] Y. Hori, Electrochemical CO_2 reduction on metal electrodes, in: C.G. Vayenas, R.E. White, M.E. Gamboa-Aldeco (Eds.), Modern Aspects of Electrochemistry, Vol. 42, Springer, 2008, pp. 89–189.

[5] S. Vesztergom, A. Dutta, M. Rahaman, K. Kiran, I.Z. Montiel, P. Broekmann, Hydrogen bubble templated metal foams as efficient catalysts of CO_2 electroreduction, ChemCatChem 13 (2020) 1039–1058, https://doi.org/10.1002/cctc.202001145.

[6] F. Yu, P. Wei, Y. Yang, Y. Chen, L. Guo, Z. Peng, Material design at nano and atomic scale for electrocatalytic CO_2 reduction, Nano, Mater. Sci. 1 (2019) 60–69, https://doi.org/10.1016/j.nanoms.2019.03.006.

[7] D. Sun, X. Xu, Y. Qin, S.P. Jiang, Z. Shao, Rational design of Ag-based catalysts for the electrochemical CO_2 reduction to CO: A review, ChemSusChem 13 (2019) 39–58, https://doi.org/10.1002/cssc.201902061.

[8] R. Reske, H. Mistry, F. Behafarid, B.R. Cuenya, P. Strasser, Particle size effects in the catalytic electroreduction of CO_2 on Cu nanoparticles, J. Am. Chem. Soc. 136 (19) (2014) 6978–6986, https://doi.org/10.1021/ja500328k.

[9] A. Dutta, A. Kuzume, V. Kaliginedi, M. Rahaman, I. Sinev, M. Ahmadi, B. Roldán Cuenya, S. Vesztergom, P. Broekmann, Probing the chemical state of tin oxide NP catalysts during CO_2 electroreduction: A complementary operando approach, Nano Energy 53 (2018) 828–840, https://doi.org/10.1016/j.nanoen.2018.09.033.

[10] Y. Hou, N. Kovács, H. Xu, C. Sun, R. Erni, M. Gálvez-Vázquez, A. Rieder, H. Hu, Y. Kong, M. Liu, B.J. Wiley, S. Vesztergom, P. Broekmann, Limitations of identical location SEM as a method of degradation studies on surfactant capped nanoparticle electrocatalysts, J. Catal. 394 (2020) 58–66, https://doi.org/10.1016/j.jcat.2020.12.006.

[11] P.C. Okonkwo, O.O. Ige, E.M. Barhoumi, P.C. Uzoma, W. Emori, A. Benamor, A. M. Abdullah, Platinum degradation mechanisms in proton exchange membrane fuel cell (PEMFC) system: A review, Int. J. Hydrog. Energy 46 (29) (2021) 15850–15865, https://doi.org/10.1016/j.ijhydene.2021.02.078.

[12] J. Huang, N. Hörmann, E. Oveisi, A. Loiudice, G.L. De Gregorio, O. Andreussi, N. Marzari, R. Buonsanti, Potential-induced nanoclustering of metallic catalysts during electrochemical CO_2 reduction, Nat. Commun. 9 (1) (2018) 3117, https://doi.org/10.1038/s41467-018-05544-3.
[13] J.R. Pankhurst, P. Iyengar, A. Loiudice, M. Mensi, R. Buonsanti, Metal–ligand bond strength determines the fate of organic ligands on the catalyst surface during the electrochemical CO_2 reduction reaction, Chem. Sci. 11 (2020) 9296–9302, https://doi.org/10.1039/d0sc03061a.
[14] S. Popović, M. Smiljanić, P. Jovanovič, J. Vavra, R. Buonsanti, N. Hodnik, Stability and degradation mechanisms of copper-based catalysts for electrochemical CO_2 reduction, Angew. Chem. 132 (35) (2020) 14844–14854, https://doi.org/10.1002/ange.202000617.
[15] M.de.J. Gálvez-Vázquez, P. Moreno-García, H. Xu, Y. Hou, H. Hu, I. Zelocualtecatl Montiel, A.V. Rudnev, S. Alinejad, V. Grozovski, B.J. Wiley, M. Arenz, P. Broekmann, Environment matters: CO_2RR electrocatalyst performance testing in a gas-fed zero-gap electrolyzer, ACS Catal. 10 (21) (2020) 13096–13108, https://doi.org/10.1021/acscatal.0c03609.
[16] H. Hu, M. Liu, Y. Kong, N. Mysuru, C. Sun, M. d. J. Gálvez-Vázquez, U. Müller, R. Erni, V. Grozovski, Y. Hou, P. Broekmann, Activation matters: Hysteresis effects during electrochemical looping of colloidal Ag nanowire catalysts, ACS Catal. 10 (2020) 8503–8514. doi:https://doi.org/10.1021/acscatal.0c02026.
[17] C.-T. Dinh, F.P.G. de Arquer, D. Sinton, E.H. Sargent, High rate, selective, and stable electroreduction of CO_2 to CO in basic and neutral media, ACS Energy Lett. 3 (2018) 2835–2840, https://doi.org/10.1021/acsenergylett.8b01734.
[18] T. Haas, R. Krause, R. Weber, M. Demler, G. Schmid, Technical photosynthesis involving CO_2 electrolysis and fermentation, Nat. Catal. 1 (2018) 32–39, https://doi.org/10.1038/s41929-017-0005-1.
[19] C.V. Restrepo, C.C. Villa, Synthesis of silver nanoparticles, influence of capping agents, and dependence on size and shape: A review, Environ. Nanotechnol. Monit. Manag. 15 (2021) 100428, https://doi.org/10.1016/j.enmm.2021.100428.
[20] R. Szűcs, D. Balogh-Weiser, E. Sánta-Bell, E. Tóth-Szeles, T. Varga, Z. Kónya, L. Poppe, I. Lagzi, Green synthesis and in situ immobilization of gold nanoparticles and their application for the reduction of p-nitrophenol in continuous-flow mode, RSC Adv. 9 (2019) 9193–9197, https://doi.org/10.1039/c8ra10373a.
[21] M. d. J. Gálvez-Vázquez, H. Xu, P. Moreno-García, Y. Hou, H. Hu, B.J. Wiley, S. Vesztergom, P. Broekmann, Unwrap them first: Operando potential-induced activation is required when using PVP-capped Ag nanocubes as catalysts of CO_2 electroreduction, Chimia 75 (2021) 163–168. doi:https://doi.org/10.2533/chimia.2021.163.
[22] J. Kieffer, J.P. Wright, PyFAI: A Python library for high performance azimuthal integration on GPU, Powder Diffr. 28 (2013) S339–S350, https://doi.org/10.1017/s0885715613000924.
[23] B.H. Toby, R.B.V. Dreele, GSAS-II: The genesis of a modern open-source all purpose crystallography software package, J. Appl. Crystallogr. 46 (2013) 544–549, https://doi.org/10.1107/s0021889813003531.
[24] J.S. Yoo, R. Christensen, T. Vegge, J.K. Nørskov, F. Studt, Theoretical insight into the trends that guide the electrochemical reduction of carbon dioxide to formic acid, ChemSusChem 9 (2015) 358–363, https://doi.org/10.1002/cssc.201501197.
[25] C. Spöri, J.T.H. Kwan, A. Bonakdarpour, D.P. Wilkinson, P. Strasser, The stability challenges of oxygen evolving catalysts: Towards a common fundamental understanding and mitigation of catalyst degradation, Angew. Chem. Int. Ed. 56 (2017) 5994–6021, https://doi.org/10.1002/anie.201608601.
[26] I. Schrader, J. Warneke, S. Neumann, S. Grotheer, A.A. Swane, J.J.K. Kirkensgaard, M. Arenz, S. Kunz, Surface chemistry of "unprotected" nanoparticles: A spectroscopic investigation on colloidal particles, J. Phys. Chem. C 119 (31) (2015) 17655–17661, https://doi.org/10.1021/acs.jpcc.5b03863.
[27] J.A.S. Bett, K. Kinoshita, P. Stoneheart, Crystallite growth of platinum dispersed on graphitized carbon black II. Effect of liquid environment, J. Catal. 41 (1976) 124–133, https://doi.org/10.1016/0021-9517(76)90207-4.
[28] P.J. Ferreira, G.J. la O', Y. Shao-Horn, D. Morgan, R. Makharia, S. Kocha, H.A. Gasteiger, Instability of Pt/C electrocatalysts in proton exchange membrane fuel cells, J. Electrochem. Soc. 152 (2005) A2256. doi:https://doi.org/10.1149/1.2050347.
[29] R. Chattot, P. Bordet, I. Martens, J. Drnec, L. Dubau, F. Maillard, Building practical descriptors for defect engineering of electrocatalytic materials, ACS Catal. 10 (2020) 9046–9056, https://doi.org/10.1021/acscatal.0c02144.